Materials Advances

ROYAL SOCIETY OF CHEMISTRY

PAPER

View Article Online
View Journal | View Issue

Check for updates

Cite this: *Mater. Adv.*, 2023, 4, 5206

Synergistic carbon and oxygen vacancy engineering on vanadium dioxide nanobelts for efficient aqueous zinc-ion batteries†

Xin Gu, * Juntao Wang, Shuang Wu, Sijin Dong, Fengchun Li, Akang Cui, Mengdi Zhang, Pengcheng Dai * and Mingbo Wu *

Vanadium-based compounds with stable crystal structures and high capacities are promising cathode materials in aqueous zinc-ion batteries (AZIBs); nevertheless, the sluggish solid-phase diffusion kinetics of zinc ions and poor electronic conductivity have obstructed their application. Herein, this study proposes a synergistic engineering approach involving carbon and oxygen vacancies to improve the performance of VO_2. Compared to VO_2, VO_2@C shows improved electron/ion transport kinetics due to carbon coating, oxygen vacancy, expanded lattice, and reduced grain size. This composite also offers improved structural stability and extra active sites, enhancing zinc-ion storage performance. The optimized VO_2@C-350 composite electrode displays a remarkable discharge capacity of 391 mA h g^{-1} at 0.1 A g^{-1} over 100 cycles and maintains good cycle stability performance at 2 A g^{-1} for over 2000 cycles. Further analysis has identified that its reaction mechanism involves a co-intercalation/de-intercalation process of the proton (H^+) and Zn^{2+}. This innovative synergistic engineering approach can be implemented in other zinc storage materials to achieve efficient AZIBs.

Received 30th August 2023,
Accepted 27th September 2023

DOI: 10.1039/d3ma00622k

rsc.li/materials-advances

Open Access Article. Published on 28 September 2023. Downloaded on 1/28/2026 1:06:22 PM.
This article is licensed under a Creative Commons Attribution-NonCommercial 3.0 Unported Licence.

1. Introduction

The importance of researching green and renewable energy has grown due to the rising concerns about energy and the environment. Consumer electronics have increasingly adopted lithium-ion batteries because of their exceptional energy density, portability, and outstanding capacity. However, the limited availability of lithium resources and safety concerns associated with flammable organic electrolytes have hindered their further development. The need for more sustainable and affordable battery options has led to the creation of post-lithium-ion batteries that utilize elements found abundantly in the earth's crust, such as Na, K, Zn, Mg, and Al.[1–6] A new and innovative water battery technology called aqueous zinc-ion batteries (AZIBs) uses a slightly acidic or near-neutral aqueous solution as an electrolyte and Zn metal as an anode. AZIBs are known for their safety, eco-friendliness, affordability, and high power capability. They have a low redox potential of −0.763 V (*vs.* H^+/H_2) and a high theoretical capacity of 820 mA h g^{-1}, making them a promising option for large-scale energy storage and smart grids.[7–9]

The cathode is an essential component in determining the energy density and cycle life of AZIBs. Various cathode hosts have been developed by researchers, including Prussian blue analogs (PBAs),[10] Mn-based,[11] V-based,[12] and organic compounds.[13] Cathode materials containing vanadium have gained significant attention due to their diverse crystal structures and valence states.[14–16] These materials possess remarkable specific capacity, exceptional rate capability, and long-lasting cycle life. Among these, B-phase vanadium dioxide (VO_2) is noteworthy for its one-dimensional tunnel structure formed by corners and edges shared by VO_6 octahedra, which supports the intercalation and delamination of Zn^{2+}.[17,18] However, VO_2 frequently faces issues such as sluggish solid-phase diffusion kinetics of zinc ions, poor electronic conductivity, and structural deterioration upon repeated ion (de)intercalation, leading to poor rate performance and a rapid decrease in capacity.[19,20] To date, numerous high-efficiency strategies have been suggested to tackle these issues. To improve the electronic conductivity and structural durability of VO_2, highly conductive carbon substrates such as graphene,[21–24] carbon cloth,[25] carbon fiber,[26] and carbon coating layer[27–30] have been utilized. Oxygen vacancy engineering has been implemented to quicken the Zn^{2+} diffusion in the solid phase and modulate the VO_2 band gap.[31–33] Nevertheless, there are only limited attempts to employ dual engineering of carbon and oxygen vacancy to enhance the electrochemical properties of VO_2. Additionally,

College of New Energy, State Key Laboratory of Heavy Oil Processing, China University of Petroleum (East China), Qingdao 266580, P. R. China.
E-mail: guxin@upc.edu.cn, dpcapple@upc.edu.cn, wumb@upc.edu.cn

† Electronic supplementary information (ESI) available. See DOI: https://doi.org/10.1039/d3ma00622k

© 2023 The Author(s). Published by the Royal Society of Chemistry

Open Access Article. Published on 28 September 2023. Downloaded on 1/28/2026 1:06:22 PM.
This article is licensed under a Creative Commons Attribution-NonCommercial 3.0 Unported Licence.

a straightforward and efficient method to simultaneously implement carbon and oxygen vacancy is urgently required.

Our study showcases a versatile and straightforward technique for producing carbon-coated VO_2 nanobelts (VO_2@C) with oxygen vacancies through C_2H_2 chemical vapor deposition. Structural and electrochemical analyses demonstrate that C_2H_2 heat treatment results in a carbon coating, oxygen vacancy, expanded lattice, and reduced grain size in VO_2, thus enabling extra active sites, accelerating electron/ion transport, and preventing structural degradation. This leads to enhanced electrochemical performance compared to pure VO_2 in AZIBs. The optimized VO_2@C-350 composite electrode displays an impressive specific capacity of 391 mA h g^{-1} at 0.1 A g^{-1} over 100 cycles. It also maintains stability at 1 and 2 A g^{-1} throughout 2000 cycles and exhibits a reliable rate performance of 174 mA h g^{-1} at 5 A g^{-1}. Our research proposes an innovative method for introducing carbon and oxygen vacancy to develop advanced cathode materials for AZIBs.

2. Experimental section

2.1 Materials synthesis

For the experiment, only analytically pure reagents were used without further purification. In order to produce vanadium dioxide, we combined 14 mmol of oxalic acid with 7 mmol of vanadium pentoxide in 40 mL of deionized water. The mixture was stirred for an hour at 75 °C before being transferred to a 50 mL Teflon autoclave and reacted at 180 °C for three hours. After producing the VO_2 nanobelts were gathered and cleaned using distilled water and ethanol before drying in a vacuum. Finally, we ensured good crystallinity by calcining them at 300 °C in the air. To produce VO_2@C-300, VO_2@C-350, and VO_2@C-400 nanobelts, the VO_2 nanobelts were subjected to calcination with a C_2H_2/Ar gas mixture (volume ratio of 1 : 9) at temperatures of 300 °C, 350 °C, and 400 °C for one hour each.

2.2 Materials characterizations

We obtained X-ray diffraction (XRD) patterns from a Panalytical X'Pert Pro MPD and X-ray photoelectron spectroscopy (XPS) results from a Thermo Scientific ESCALAB 250Xi instrument. To carry out XRD and XPS tests *ex situ*, we dismantled cells at specific voltages and thoroughly rinsed them with distilled water multiple times. Afterward, we dried them in a vacuum to prepare the electrodes. We captured visuals of the specimens with field-emission transmission electron microscopy (TEM, JEOL-2100F), energy dispersion X-ray spectroscopy (EDS), and field-emission scanning electron microscopy (SEM, JEOL JSM-7500F). We used a NEXUS 670 Raman spectrometer with a 532 nm excitation source to acquire Raman spectra. We used a TG-DTA STA409PC thermogravimetric analyzer to perform thermogravimetric analysis (TGA) on the samples. Additionally, we adopted an EPR spectrometer (A300-10-12, Bruker) to conduct room temperature electron paramagnetic resonance (EPR) tests on the samples, using a 9.45 GHz x-band with an amplitude of 5.00 g modulation and 100 kHz magnetic field modulation.

2.3 Electrochemical measurements

A consistent blend of VO_2@C, acetylene black, and polyvinylidene difluoride (PVDF) in a 7 : 2 : 1 weight ratio was utilized to make a cathode slurry. We applied the slurry onto a Ti foil and dried it under a vacuum at 120 °C. We cut the dried foil into disks that were 12 mm in diameter, which gave an active material mass loading of around 1 mg cm^{-2}. We used zinc foil for the anodes, 3 M $Zn(CF_3SO_3)_2$ aqueous solution for the electrolytes, and Whatman glass microfiber (GF/D) for the separators. We assembled CR2032 coin cells under an air atmosphere with an electrolyte drop volume of 120 μL to evaluate the electrochemical performance. To perform cyclic voltammetry (CV) tests, we utilized a CHI760E electrochemical workstation (Shanghai Chenhua). Additionally, we conducted galvanostatic charge/discharge measurements on a LAND-CT2001A battery cycler at different current densities. We used The voltage window between 0.25 and 1.4 V compared to Zn^{2+}/Zn. For the electrochemical impedance spectroscopy (EIS) measurements, we utilized a Gamry-Reference 3000 electrochemical workstation. The measurements were conducted across a 100 kHz to 0.01 Hz frequency range. Before completing the EIS measurements, we cycled the electrodes for 10 cycles at 0.1 A g^{-1}. To calculate zinc-ion diffusion coefficients ($D_{Zn^{2+}}$), we employed eqn (1).

$$D_{Zn^{2+}} = \frac{R^2T^2}{2A^2n^4F^4C^2\sigma^2} \quad (1)$$

Eqn (1) includes different variables such as σ, representing the Warburg factor, F for the Faraday constant, C for the zinc-ion concentration, A for the electrode surface area, T for the absolute temperature, n for the number of electrons per molecule, and R for the gas constant. To determine the value of σ, one can calculate the line slope using eqn (2).

$$Z' = R_D + R_L + \sigma\omega^{-1/2} \quad (2)$$

We conducted galvanostatic intermittent titration technique (GITT) tests to determine the diffusion coefficient of Zn^{2+} in the electrode. As part of the GITT tests, participants were instructed to cycle for 20 minutes at 50 mA g^{-1} and rest for 2 hours after completing 10 activation cycles. During each relaxation period, the potential change indicated the overpotential of the corresponding discharge/charge state. To determine $D_{Zn^{2+}}$, we employed Fick's second law and used a simplified equation.

$$D_{Zn^{2+}} = \frac{4}{\pi\tau}\left(\frac{m_BV_M}{M_BS}\right)^2\left(\frac{\Delta E_S}{\Delta E_\tau}\right)^2 \left(\tau \ll L^2/D_{Zn^{2+}}\right) \quad (3)$$

Eqn (3) includes various factors such as the mass of the electrode material (m_B), its molar mass (M_B), molar volume (V_M), geometric area (S), potential equilibrium difference (ΔE_s), change in cell voltage due to impulse current (ΔE_τ), and average thickness of the electrode (L).

Open Access Article. Published on 28 September 2023. Downloaded on 1/28/2026 1:06:22 PM.
This article is licensed under a Creative Commons Attribution-NonCommercial 3.0 Unported Licence.

3. Results and discussion

The process of creating VO_2@C nanobelts is shown in Fig. 1(a). The initial step involves producing pure VO_2 nanobelts through a hydrothermal reaction using vanadium pentoxide and oxalic acid as reagents. Subsequently, these nanobelts undergo calcination in the air. The next step involves the calcination of VO_2 nanobelts with mixed C_2H_2/Ar under varying temperatures to create VO_2@C nanobelts with different microstructures. SEM and TEM measurements were carried out to examine the microstructures and morphologies of VO_2-based samples. Fig. 1(b) displays the nanobelt structure of pure VO_2, with the belt width ranging from 50–150 nm. The nanobelt architecture shows no changes after undergoing C_2H_2 heat treatment for VO_2@C-300, VO_2@C-350, and VO_2@C-400 (Fig. 1(c)–(e)). Upon analysis of the high-resolution TEM (HRTEM) images of VO_2@C-350 (Fig. 1(f) and (g)), it can be confirmed that the core–shell nanobelt structure has indeed been formed after the C_2H_2 heat treatment, and the carbon coating thickness on the sample after calcination at 350 °C is approximately 2 nm. A lattice stripe, with an interplanar spacing of 0.616 nm, is also visible, aligning with the (001) VO_2(B) plane (Fig. 1(g)). In addition, the EDS pattern of VO_2@C-350 displays an even dispersion of V, O, and C components throughout its composition, as depicted in Fig. 1(h). The VO_2@C-300 and VO_2@C-400 samples were also subjected to HRTEM and EDS characterizations. Despite the relatively low calcination temperature, EDS maps confirm the existence of a carbon coating layer on VO_2@C-300, albeit barely visible, as shown in Fig. S1 (ESI†). In contrast, the carbon layer on VO_2@C-400 grows considerably, measuring around 4 to 20 nm, as observed in Fig. S2 (ESI†).

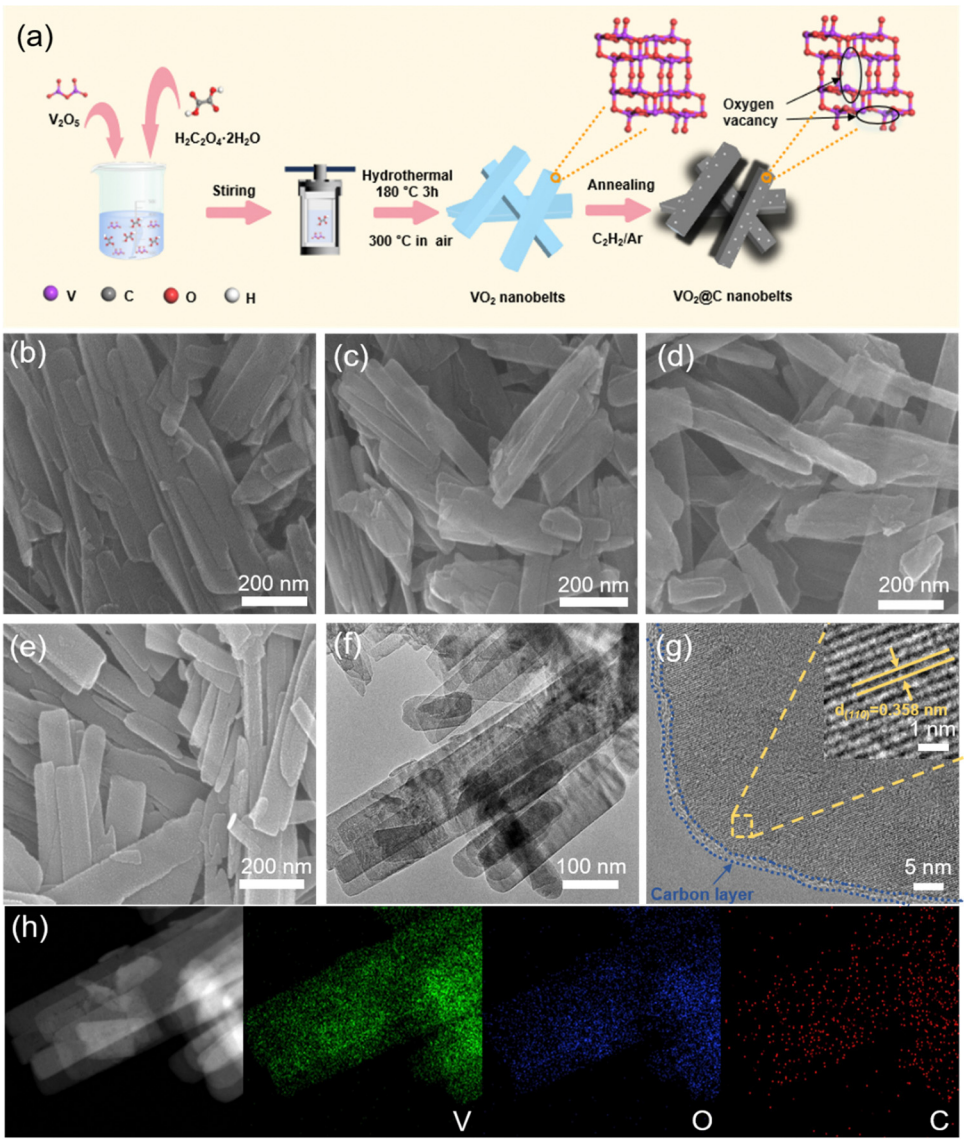

Fig. 1 (a) Scheme of the synthesis process for VO_2@C nanobelts. SEM images for (b) VO_2, (c) VO_2@C-300, (d) VO_2@C-350, and (e) VO_2@C-400. (f) and (g) HRTEM images, and (h) EDS maps of VO_2@C-350.

© 2023 The Author(s). Published by the Royal Society of Chemistry

Open Access Article. Published on 28 September 2023. Downloaded on 1/28/2026 1:06:22 PM.
This article is licensed under a Creative Commons Attribution-NonCommercial 3.0 Unported Licence.

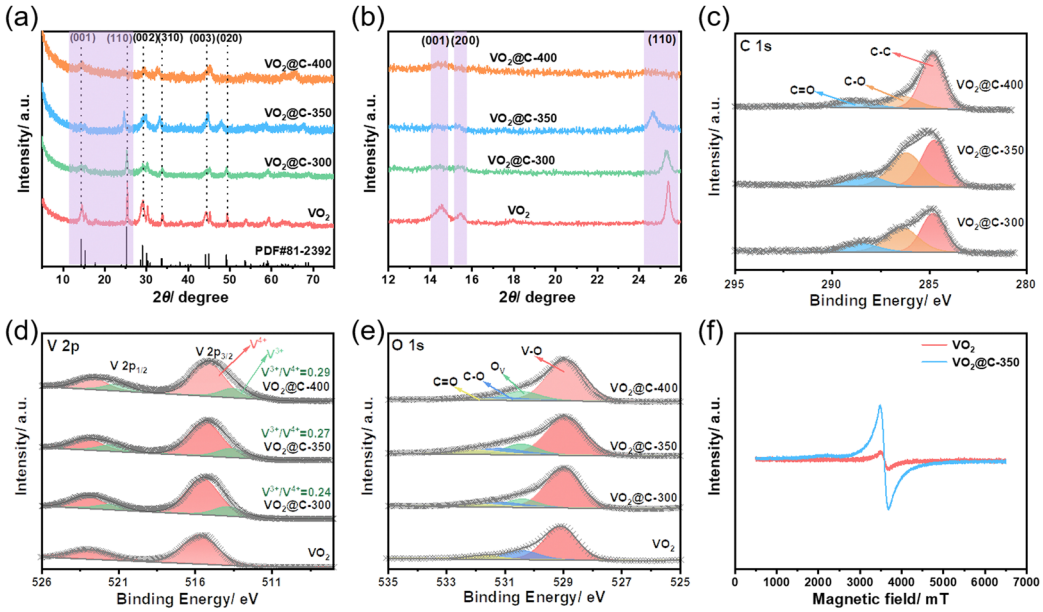

Fig. 2 Structural characterizations of VO_2-based samples. (a) and (b) XRD patterns, (c)–(e) high-resolution C 1s, V 2p, and O 1s XPS spectra, and (f) EPR spectra.

The VO_2-based samples' crystal structures were analyzed using XRD. In Fig. 2(a), the XRD patterns of these samples are shown. It can be observed that all diffraction peaks correspond to VO_2(B) (JCPDS no. 81-2392) having the space group of *C*2/*m*. Moreover, no noticeable impurities have been observed either before or after the C_2H_2 heat treatment. By analyzing the zoomed-in view of XRD patterns shown in Fig. 2(b), the diffraction peaks' intensity decreases as the calcination temperature increases. This decrease in intensity suggests a reduction in crystallinity. Additionally, the characteristic peak (110) is observed to broaden and shift to a lower angle, indicating a decrease in grain size and an increase in interlayer spacing. These changes favor embedding and exfoliating zinc ions during discharging/charging. In Fig. S3 (ESI†), we can observe the Raman spectra of VO_2-based samples. The peaks detected at 148, 288, 414, 530, and 997 cm^{-1} in VO_2 indicate stretching and bending vibrations between the V–O within the layers.[30,34] Additionally, the peak at 697 cm^{-1} shows the coordination of the vanadium atom with three oxygen atoms.[22] Interestingly, the vibration patterns of VO_2@C samples are comparable to those of the original VO_2, suggesting that VO_2's crystal structure remains intact after the C_2H_2 heat treatment. In addition, the presence of D and G bands in VO_2@C samples confirms the formation of carbon.

An XPS analysis examined the samples' electronic structure and surface composition. Based on the XPS survey spectra (shown in Fig. S4, ESI†), it can be determined that all VO_2@C samples contain V, O, and C elements. The spectra of the VO_2@C samples in Fig. 2(c) show three distinct peaks at 284.8, 286.2, and 288.4 eV in the C 1s region. These peaks indicate the presence of C–C, C–O, and C═O bonds, respectively. These findings suggest that carbon has been successfully introduced.[35,36] Pure VO_2 exhibits two peaks at 515.8 and 522.8 eV in the V 2p spectrum, indicating the presence of V^{4+} in VO_2, as depicted in Fig. 2(d).[23] Following the C_2H_2 heat treatment, it was observed that the VO_2@C samples displayed two additional peaks at 513.6 and 521.1 eV, which corresponded to V^{3+}, indicating the formation of oxygen vacancies in VO_2.[32] The area ratios of V^{3+}/V^{4+} calculated for VO_2@C-300, VO_2@C-350, and VO_2@C-400 are 0.24, 0.27, and 0.29, respectively. These results indicate that the proportion of V^{3+} increases gradually with increasing calcination temperature, leading to an increase in the content of oxygen vacancies in the samples. The presence of these vacancies facilitates the rapid migration of ions and provides more channels for ion migration. From the O 1s spectra illustrated in Fig. 2(e), it can be inferred that the VO_2@C samples contain oxygen vacancies. The peaks at 529.6, 531.1, 531.8, and 532.4 eV signify V–O, oxygen vacancy (O_v), C–O, and C═O, respectively.[32] Further evidence of the presence of oxygen vacancies was obtained through EPR spectroscopy, as shown in Fig. 2(f). The signal of VO_2@C-350 exhibits a more pronounced symmetry peak at g = 2.0 compared to VO_2. This is generally attributed to the presence of oxygen vacancy. TGA was utilized to determine the carbon mass fraction in the VO_2@C composites produced at various temperatures, and the results are shown in Fig. S5 (ESI†). During heating in the air at a ramp rate of 10 °C per minute to 700 °C, there was a weight loss observed up to 200 °C. This was attributed to the loss of adsorbed water. C was converted to CO_2 as the temperature increased, and VO_2 was oxidized to V_2O_5.[21,22] As a result, VO_2@C-300, VO_2@C-350, and VO_2@C-400 have a carbon content of approximately 3.2, 5.1, and 16.5 wt%, respectively. These findings align with the carbon layer thickness observed on HRTEM.

We conducted a study to evaluate the Zn storage performance of VO_2-based samples using a coin cell model (Fig. 3) to

Open Access Article. Published on 28 September 2023. Downloaded on 1/28/2026 1:06:22 PM.
This article is licensed under a Creative Commons Attribution-NonCommercial 3.0 Unported Licence.

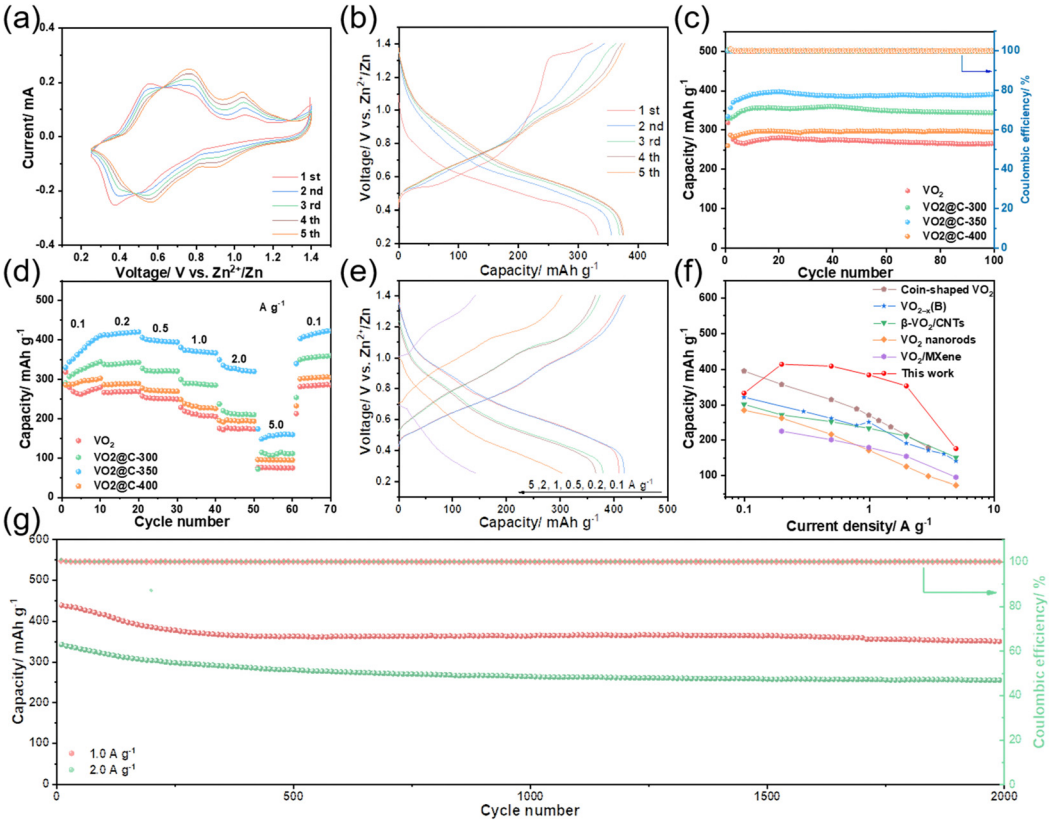

Fig. 3 Zn storage performance of VO_2-based samples. (a) CV curves of VO_2@C-350 at 0.2 mV s^{-1}. (b) Charge/discharge curves of VO_2@C-350 at 0.1 A g^{-1}. (c) Cycle performance and CEs of VO_2-based samples at 0.1 A g^{-1}. (d) Rate performance of VO_2-based samples. (e) Charge/discharge profiles of VO_2@C-350 at 0.1 to 5 A g^{-1}. (f) Comparison of VO_2@C-350 with other VO_2-based cathode materials for AZIBs. (g) Long cycle performance of VO_2@C-350.

assess how oxygen vacancy and carbon coating affect the properties. In Fig. 3(a), the CV curves of VO_2@C-350 are displayed at a scan rate of 0.2 mV s^{-1}, ranging from 0.25 to 1.4 V. Based on our research, it appears that there is a notable redox coupling occurring at 0.37/0.56 and 0.92/1.05 V. This finding indicates a potential two-step zinc-ion (de)intercalation mechanism.[20] Upon conducting the initial two scans, we observe stable redox couples, showing a remarkably reversible (de)intercalation reaction of Zn^{2+}. The voltage curve for VO_2@C-350's Zn storage process at 0.1 A g^{-1} is depicted in Fig. 3(b). In the initial cycle; the cell experiences an activation reaction that cannot be reversed. During the subsequent processes, two significant cathodic/anodic platforms occur at around 0.6/0.7 and 0.9/1.0 V, corresponding to the zinc ions' (de)intercalation process. This is consistent with the findings derived from the analysis of the CV. In Fig. 3(c), the performance of VO_2, VO_2@C-300, VO_2@C-350, and VO_2@C-400 in terms of cycle performance and Coulombic efficiency (CE) at 0.1 A g^{-1} is demonstrated. Unfortunately, pure VO_2 does not display good electrochemical activity, with an initial discharge capacity of only 319 mA h g^{-1}. However, VO_2@C-300 and VO_2@C-350 show improved electrochemical activity with initial discharge capacities of 330 and 335 mA h g^{-1} after carbon cladding. Interestingly, VO_2@C-400, with substantial carbon cladding, only delivers 260 mA h g^{-1} discharge capacity. Based on the VO_2@C samples, there appears to be a gradual increase in the first few cycles, possibly attributed to the activation process of the electrodes. After 100 cycles, it has been observed that VO_2@C-350 shows the highest electrochemical stability among the samples. It has a discharge capacity of around 391 mA h g^{-1} and no capacity decay. At the same time, the CE of C@VO_2-350 is maintained at 99.5% throughout the cycles. After 100 cycles, pure VO_2 has a capacity retention rate of 83.4%, with its capacity dropping to only 266 mA h g^{-1}. In Fig. 3(d), we can see the rate performance of different samples at varying currents of 0.1 to 5 A g^{-1}. Out of all the samples, VO_2@C-350 has the most impressive rate performance. It can deliver discharge capacities of 331, 413, 406, 381, 350, and 174 mA h g^{-1} at 0.1, 0.2, 0.5, 1.0, 2.0, and 5.0 A g^{-1}. It's important to note that the VO_2@C-350's capacity remains consistent even when the rate drops abruptly to 0.1 A g^{-1}. Fig. 3(e) displays the voltage curves for the discharge and charge of VO_2@C-350. Furthermore, according to the data presented in Fig. 3(f), VO_2@C-350 exhibits a higher rate performance compared to other cathodes that are based on VO_2 for AZIBs, such as VO_{2-x}(B),[37] coin-shaped VO_2,[38] VO_2 nanorods,[39] β-VO_2/CNTs,[40] and VO_2/Mxene.[41] In Fig. 3(g), the performance of VO_2@C-350 is observed throughout a lengthy cycling period, with its corresponding CE at 1 and 2 A g^{-1}.

© 2023 The Author(s). Published by the Royal Society of Chemistry

Open Access Article. Published on 28 September 2023. Downloaded on 1/28/2026 1:06:22 PM.
This article is licensed under a Creative Commons Attribution-NonCommercial 3.0 Unported Licence.

Before the high-current test, the electrodes are activated with a slight current density of 0.1 A g^{-1}. At a rate of 1 A g^{-1}, the initial capacity is 438 mA h g^{-1}, while at 2 A g^{-1}, it is 342 mA h g^{-1}. After undergoing 2000 cycles, the VO_2@C-350 exhibits a discharge capacity of 350 and 254 mA h g^{-1} while maintaining 98.7% and 99.2% CE, respectively. These findings demonstrate the impressive cycling stability of VO_2@C-350, indicating that the carbon cladding layer and oxygen vacancy can enhance conductivity and preserve the electrode material's structure.

Using EIS testing, it was discovered that VO_2@C-350 had better reaction kinetics than the other materials. The Nyquist plots for these VO_2-based samples exhibit comparable features (Fig. 4(a)). They all show a semi-circle that represents the charge transfer resistance (R_{ct}) of the electrode/electrolyte interface, along with a straight line that denotes the Warburg impedance (Z_w). According to Table S1 (ESI†), VO_2@C-350 has a charge transfer resistance of only 92.2 Ω, which is lower than VO_2 (119.1 Ω), VO_2@C-300 (100.4 Ω), and VO_2@C-400 (127.3 Ω). This suggests that VO_2@C-350 has superior charge transfer kinetics. Fig. 4(b) illustrates a correlation between Z' and $\omega^{-1/2}$ in the low-frequency range. The Warburg factor (σ), which represents the slope of the line, shows a direct correlation with $D_{Zn^{2+}}$. After evaluating the Warburg factor, we were able to determine the diffusion coefficient of Zn^{2+} to be 9.7 × 10^{-11} cm^2 s^{-1} for VO_2, 1.7 × 10^{-10} cm^2 s^{-1} for VO_2@C-300, 2.7 × 10^{-9} cm^2 s^{-1} for VO_2@C-350, and 1.3 × 10^{-10} cm^2 s^{-1} for VO_2@C-400 (refer to Table S1, ESI†). We performed GITT measurements to evaluate $D_{Zn^{2+}}$ in electrodes made from VO_2. Fig. S6 (ESI†) displays the curves for voltage response and $D_{Zn^{2+}}$ for VO_2, VO_2@C-300, VO_2@C-350, and VO_2@C-400, as well as their associated discharge/charge states. Based on the EIS analysis and GITT measurements, the order of $D_{Zn^{2+}}$ in the electrodes appears as follows: VO_2@C-350 > VO_2@C-300 > VO_2@C-400 > VO_2. From the results, we can conclude that VO_2@C-350 exhibits outstanding charge transfer and zinc-ion diffusion kinetics due to its optimized structure. Compared to the other samples, this contributes to its ability to achieve the highest storage capacity for Zn ions, cycling durability, and rate capability. We conducted CV tests on VO_2@C-350 to determine the extent of diffusion-controlled and capacitance-controlled Zn ion storage. The results, displayed in Fig. 4(c), show that the CV curves of VO_2@C-350 have similar shapes at 0.1–0.5 mV s^{-1}. When the scan rate increases, the oxidation peak moves towards higher voltages, and the reduction peak moves towards lower voltages. The equation $i = av^b$ determines the peak current (i) based on the sweep frequency (v), with parameters a and b. When the value of b approaches 0.5, it suggests that ion diffusion processes are the primary factor influencing capacity. On the other hand, when b approaches 1, capacitive processes play a more significant role in determining capacity. By applying a logarithmic transformation to the current–sweep relationship shown in Fig. 4(d), the values of b for peaks 1, 2, 3, and 4 can be computed as 0.99, 0.86, 0.94, and 1.14, respectively. These values suggest that the pseudocapacitance contribution of VO_2@C-350 is present throughout the redox process. An equation is used to determine the capacitance contribution: $i = k_1v + k_2v^{1/2}$. The equation includes k_1 and k_2, which serve as percentage coefficients for the capacitance and diffusion factors in the overall capacity calculation. According to Fig. 4(e), the level of capacitance contribution rises considerably as the scan rate increases, resulting in advantageous outcomes for quick Zn^{2+} storage and cycle durability. According to the data shown in Fig. 4(f), when the scan rate is set at 0.5 mV s^{-1},

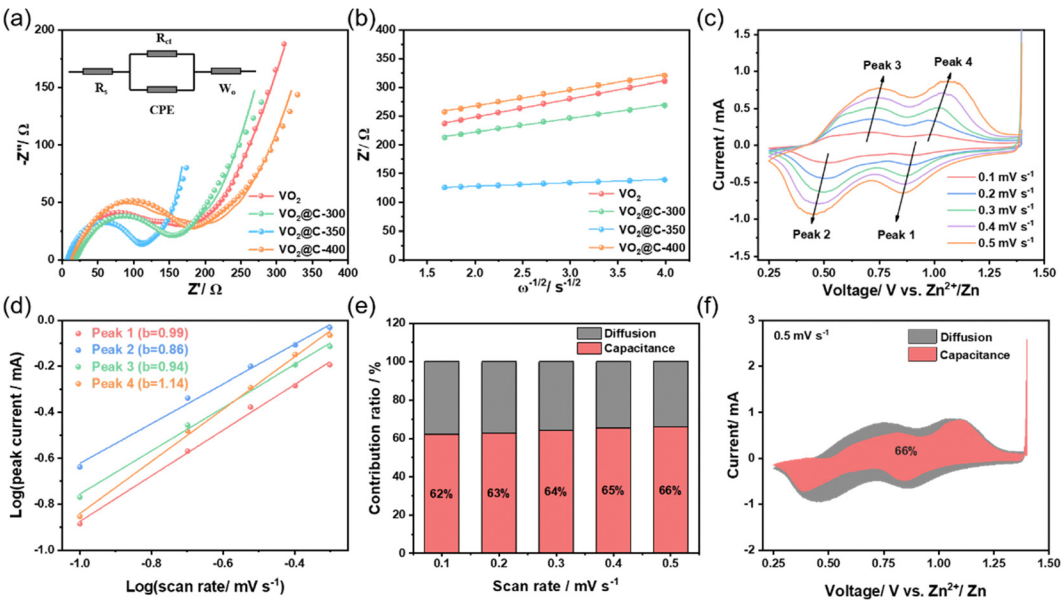

Fig. 4 (a) Nyquist plots and equivalent circuit of VO_2-based samples. (b) Correlation between Z' and $\omega^{-1/2}$. (c) CV curves for VO_2@C-350 at 0.1–0.5 mV s^{-1}. (d) Log(i) *versus* log(v) plots of VO_2@C-350. (e) Contribution of capacitive ion storage of VO_2@C-350 at 0.1–0.5 mV s^{-1}. (f) Contribution of capacitive ion storage of VO_2@C-350 at 0.5 mV s^{-1}.

Open Access Article. Published on 28 September 2023. Downloaded on 1/28/2026 1:06:22 PM.
This article is licensed under a Creative Commons Attribution-NonCommercial 3.0 Unported Licence.

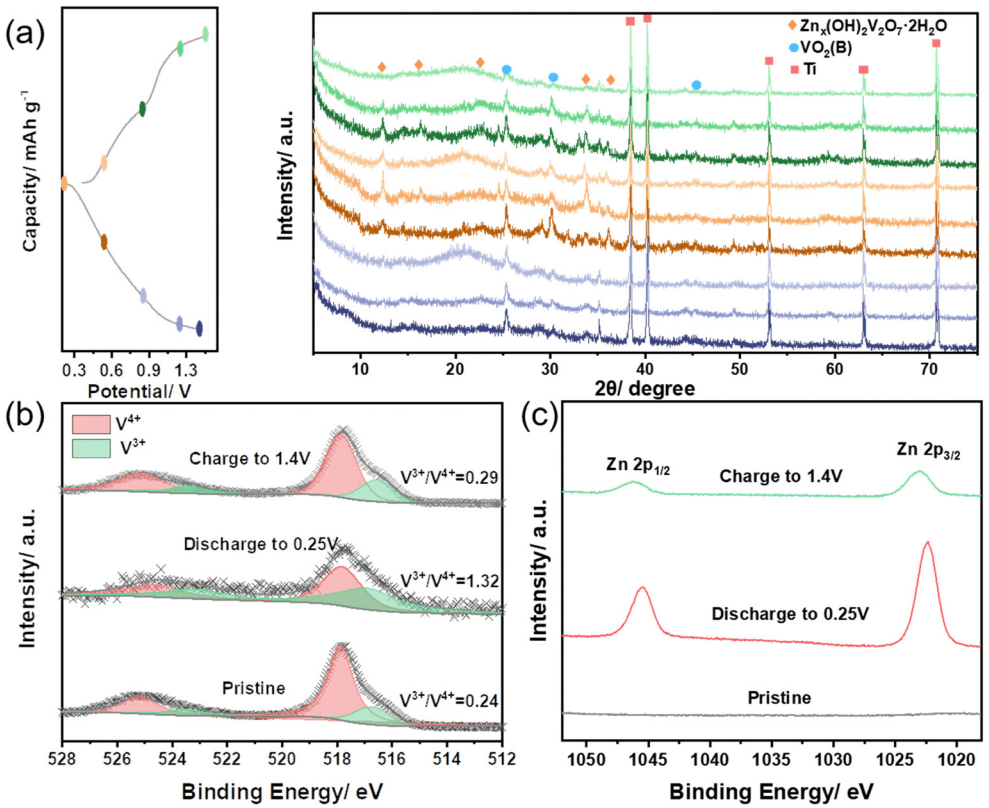

Fig. 5 *Ex situ* structural characterizations of VO_2@C-350 electrode in the 1st cycle. (a) XRD patterns, (b) V 2p XPS spectra, and (c) Zn 2p XPS spectra.

the capacitance contribution reaches its peak at 66%. Moreover, we analyzed the Zn storage in the electrodes of VO_2, VO_2@C-300, and VO_2@C-400 by employing the same analytical method. The results in Fig. S7–S9 (ESI†) indicate that the VO_2@C-350 electrode exhibits a much higher capacitance contribution than the VO_2 and VO_2@C-300 electrodes. This highlights the superior performance of the VO_2@C-350 electrode. Our research shows that the samples demonstrate a blend of ion storage mechanisms controlled by both capacitive and diffusion processes. Additionally, we observed that introducing oxygen vacancy and carbon coating into VO_2 facilitated zinc-ion adsorption/desorption behavior.

We carried out *ex situ* XRD and XPS investigations to gain insights into the process of zinc-ion storage in VO_2@C-350 (Fig. 5). In the first cycle, Fig. 5(a) displays *ex situ* XRD patterns of the VO_2@C-350 electrode. The pristine electrode displays distinct diffraction peaks, including 25.3, 30.0, and 44.9°, which correspond to the crystal planes (110), (−401), and (−601) of VO_2(B). Notably, the peaks observed during charging/discharging are consistently present, which suggests that the zinc-ion storage of VO_2@C-350 is highly reversible and that the structural stability of the material is excellent. Moreover, new heights appear at 12.4 and 36.1° during discharge, which can be attributed to the $Zn_x(OH)_2V_2O_7{\cdot}2H_2O$ species.[24,42] It seems that introducing zinc ions triggers a new phase, while their removal causes it to disappear. This implies that zinc storage relies on a co-intercalation/de-intercalation process of the Zn^{2+} and proton (H^+). Fig. 5(b) displays the V 2p spectra of the VO_2@C-350 electrode at different states. The ratio of V^{3+}/V^{4+} in the pristine electrode is 0.24, which increases to 1.32 following discharge to 0.25 V due to H^+/Zn^{2+} intercalation. Once charged to 1.4 V, the ratio of V^{3+}/V^{4+} almost returns to its initial state. This indicates a reversible extraction of H^+/Zn^{2+} from the VO_2@C-350 structure. The Zn 2p spectrum (Fig. 5(c)) also supports this conclusion, as no Zn elemental is observed in the pristine electrode before charging and discharging. The Zn signal is significantly reduced during charging compared to the peaks during discharge, indicating that Zn^{2+} is extracted from VO_2@C-350. However, trace Zn peak signals may be attributed to residual electrolytes on the electrode surface and irreversible Zn^{2+} intercalation in the VO_2@C-350 electrode even after charging. Based on *ex situ* XRD and XPS analysis, it has been determined that VO_2@C-350 exhibits an H^+/Zn^{2+} storage process that follows a (de)intercalation reaction mechanism.

4. Conclusions

We synthesized VO_2@C composites with oxygen vacancies using C_2H_2 heat treatment. The composites underwent evaluation as possible AZIB cathodes. The VO_2@C-350 electrode, which was optimized, displayed remarkable ion storage capacity, boasting a specific capacity of 391 mA h g^{-1} at 0.1 A g^{-1} over 100 cycles and stable cycle performance at 1 and 2 A g^{-1} throughout 2000 cycles.

© 2023 The Author(s). Published by the Royal Society of Chemistry

Open Access Article. Published on 28 September 2023. Downloaded on 1/28/2026 1:06:22 PM.
This article is licensed under a Creative Commons Attribution-NonCommercial 3.0 Unported Licence.

Based on experimental findings, the remarkable electrochemical capabilities of VO_2@C-350 can be traced back to its improved charge transfer, heightened ion transportation, and better pseudocapacitive properties. Furthermore, *ex situ* XRD and XPS analyses discovered that H^+/Zn^{2+} storage in VO_2@C-350 follows a (de)intercalation reaction mechanism.

Conflicts of interest

There are no conflicts to declare.

Acknowledgements

We want to express our gratitude for the financial assistance provided by various sources. These include the Natural Science Foundation of Shandong Province (ZR2022MB088), the National Natural Science Foundation of China (22378426 and 22138013), the Taishan Scholar Project (ts201712020), and the Innovation and Entrepreneurship Training Program for college students at China University of Petroleum (East China) (202207011).

References

1 Y. Chu, J. Zhang, Y. Zhang, Q. Li, Y. Jia, X. Dong, J. Xiao, Y. Tao and Q.-H. Yang, Reconfiguring Hard Carbons with Emerging Sodium-ion Batteries: a Perspective, *Adv. Mater.*, 2023, 2212186, DOI: 10.1002/adma.202212186.
2 J. Ge, L. Fan, A. M. Rao, J. Zhou and B. Lu, Surface-substituted Prussian blue analogue cathode for sustainable potassium-ion batteries, *Nat. Sustain.*, 2022, **5**, 225–234.
3 M. Li, Z. Li, X. Wang, J. Meng, X. Liu, B. Wu, C. Han and L. Mai, Comprehensive understanding of the roles of water molecules in aqueous Zn-ion batteries: from electrolytes to electrode materials, *Energy Environ. Sci.*, 2021, **14**, 3796–3839.
4 Y. Zhu, X. Guo, Y. Lei, W. Wang, A.-H. Emwas, Y. Yuan, Y. He and H. N. Alshareef, Hydrated eutectic electrolytes for high-performance Mg-ion batteries, *Energy Environ. Sci.*, 2022, **15**, 1282–1292.
5 Y. Yang, J. Zhou, L. Wang, Z. Jiao, M. Xiao, Q.-A. Huang, M. Liu, Q. Shao, X. Sun and J. Zhang, Prussian blue and its analogues as cathode materials for Na-, K-, Mg-, Ca-, Zn- and Al-ion batteries, *Nano Energy*, 2022, **99**, 107424.
6 X. Gu, L. Zhang, W. Zhang, S. Liu, S. Wen, X. Mao, P. Dai, L. Li, D. Liu, X. Zhao and Z. Guo, A CoSe–C@C core–shell structure with stable potassium storage performance realized by an effective solid electrolyte interphase layer, *J. Mater. Chem. A*, 2021, **9**, 11397–11404.
7 S. Liu, L. Kang, J. M. Kim, Y. T. Chun, J. Zhang and S. C. Jun, Recent Advances in Vanadium-Based Aqueous Rechargeable Zinc-Ion Batteries, *Adv. Energy Mater.*, 2020, **10**, 2000477.
8 M. Wu, G. Zhang, H. Yang, X. Liu, M. Dubois, M. A. Gauthier and S. Sun, Aqueous Zn-based rechargeable batteries: Recent progress and future perspectives, *InfoMat*, 2022, **4**, e12265.
9 L. E. Blanc, D. Kundu and L. F. Nazar, Scientific Challenges for the Implementation of Zn-Ion Batteries, *Joule*, 2020, **4**, 771–799.
10 Y. Li, J. Zhao, Q. Hu, T. Hao, H. Cao, X. Huang, Y. Liu, Y. Zhang, D. Lin, Y. Tang and Y. Cai, Prussian blue analogs cathodes for aqueous zinc ion batteries, Mater. Today, *Energy*, 2022, **29**, 101095.
11 T. Xiong, Y. Zhang, W. S. V. Lee and J. Xue, Defect Engineering in Manganese-Based Oxides for Aqueous Rechargeable Zinc-Ion Batteries: A Review, *Adv. Energy Mater.*, 2020, **10**, 2001769.
12 X. Chen, H. Zhang, J.-H. Liu, Y. Gao, X. Cao, C. Zhan, Y. Wang, S. Wang, S.-L. Chou, S.-X. Dou and D. Cao, Vanadium-based cathodes for aqueous zinc-ion batteries: Mechanism, design strategies and challenges, *Energy Storage Mater.*, 2022, **50**, 21–46.
13 Z. Guo, Y. Ma, X. Dong, J. Huang, Y. Wang and Y. Xia, An Environmentally Friendly and Flexible Aqueous Zinc Battery Using an Organic Cathode, *Angew. Chem., Int. Ed.*, 2018, **57**, 11737–11741.
14 X. Xu, Y. Qian, C. Wang, Z. Bai, C. Wang, M. Song, Y. Du, X. Xu, N. Wang, J. Yang, Y. Qian and S. Dou, Enhanced charge transfer and reaction kinetics of vanadium pentoxide for zinc storage via nitrogen interstitial doping, *Chem. Eng. J.*, 2023, **451**, 138770.
15 S. Deng, Z. Yuan, Z. Tie, C. Wang, L. Song and Z. Niu, Electrochemically Induced Metal-Organic-Framework-Derived Amorphous V(2) O(5) for Superior Rate Aqueous Zinc-Ion Batteries, *Angew. Chem., Int. Ed.*, 2020, **59**, 22002–22006.
16 Z. Li, L. Wu, S. Dong, T. Xu, S. Li, Y. An, J. Jiang and X. Zhang, Pencil Drawing Stable Interface for Reversible and Durable Aqueous Zinc-Ion Batteries, *Adv. Funct. Mater.*, 2020, **31**, 2006495.
17 J. Ding, Z. Du, L. Gu, B. Li, L. Wang, S. Wang, Y. Gong and S. Yang, Ultrafast Zn(2+) Intercalation and Deintercalation in Vanadium Dioxide, *Adv. Mater.*, 2018, **30**, e1800762.
18 L. Chen, Y. Ruan, G. Zhang, Q. Wei, Y. Jiang, T. Xiong, P. He, W. Yang, M. Yan, Q. An and L. Mai, Ultrastable and High-Performance Zn/VO_2 Battery Based on a Reversible Single-Phase Reaction, *Chem. Mater.*, 2019, **31**, 699–706.
19 J. Guo, L. Li, J. Luo, W. Gong, R. Pan, B. He, S. Xu, M. Liu, Y. Wang, B. Zhang, C. Wang, L. Wei, Q. Zhang and Q. Li, Polypyrrole-Assisted Nitrogen Doping Strategy to Boost Vanadium Dioxide Performance for Wearable Nonpolarity Supercapacitor and Aqueous Zinc-Ion Battery, *Adv. Energy Mater.*, 2022, **12**, 2201481.
20 X. Gu, J. Wang, X. Zhao, X. Jin, Y. Jiang, P. Dai, N. Wang, Z. Bai, M. Zhang and M. Wu, Engineered nitrogen doping on VO_2(B) enables fast and reversible zinc-ion storage capability for aqueous zinc-ion batteries, *J. Energy Chem.*, 2023, **85**, 30–38.
21 X. Dai, F. Wan, L. Zhang, H. Cao and Z. Niu, Freestanding graphene/VO_2 composite films for highly stable aqueous Zn-ion batteries with superior rate performance, *Energy Storage Mater.*, 2019, **17**, 143–150.

© 2023 The Author(s). Published by the Royal Society of Chemistry

Open Access Article. Published on 28 September 2023. Downloaded on 1/28/2026 1:06:22 PM. This article is licensed under a Creative Commons Attribution-NonCommercial 3.0 Unported Licence.

22 D. Jia, K. Zheng, M. Song, H. Tan, A. Zhang, L. Wang, L. Yue, D. Li, C. Li and J. Liu, $VO_2{\cdot}0.2H_2O$ nanocuboids anchored onto graphene sheets as the cathode material for ultrahigh capacity aqueous zinc ion batteries, *Nano Res.*, 2020, **13**, 215–224.

23 F. Cui, J. Zhao, D. Zhang, Y. Fang, F. Hu and K. Zhu, VO_2(B) nanobelts and reduced graphene oxide composites as cathode materials for low-cost rechargeable aqueous zinc ion batteries, *Chem. Eng. J.*, 2020, **390**, 124118.

24 H. Luo, B. Wang, C. Wang, F. Wu, F. Jin, B. Cong, Y. Ning, Y. Zhou, D. Wang, H. Liu and S. Dou, Synergistic deficiency and heterojunction engineering boosted VO_2 redox kinetics for aqueous zinc-ion batteries with superior comprehensive performance, *Energy Storage Mater.*, 2020, **33**, 390–398.

25 P. Luo, W. Zhang, W. Cai, Z. Huang, G. Liu, C. Liu, S. Wang, F. Chen, L. Xia, Y. Zhao, S. Dong and L. Xia, Accelerated ion/electron transport kinetics and increased active sites via local internal electric fields in heterostructured VO_2-carbon cloth for enhanced zinc-ion storage, *Nano Res.*, 2022, **16**, 503–512.

26 X. Li, L. Yang, H. Mi, H. Li, M. Zhang, A. Abliz, F. Zhao, S. Wang and H. Li, VO_2(B)@carbon fiber sheet as a binder-free flexible cathode for aqueous Zn-ion batteries, *CrystEngComm*, 2021, **23**, 8650–8659.

27 M. Yang, D. Ma, H. Mi, X. Yang, Y. Wang, L. Sun and P. Zhang, A unique morphology and interface dual-engineering strategy enables the holey C@VO_2 cathode with enhanced storage kinetics for aqueous Zn-ion batteries, *J. Mater. Chem. A*, 2021, **9**, 8792–8804.

28 Y. Liu, Y. Liu, X. Wu and Y. R. Cho, Enhanced Electrochemical Performance of Zn/VO(x) Batteries by a Carbon-Encapsulation Strategy, *ACS Appl. Mater. Interfaces*, 2022, **14**, 11654–11662.

29 T.-T. Lv, X. Luo, G.-Q. Yuan, S.-Y. Yang and H. Pang, Layered VO_2@N-doped carbon composites for high-performance rechargeable aqueous zinc-ion batteries, *Chem. Eng. J.*, 2022, **428**, 131211.

30 M. Yang, Y. Wang, Z. Sun, H. Mi, S. Sun, D. Ma and P. Zhang, Anti-aggregation growth and hierarchical porous carbon encapsulation enables the C@VO_2 cathode with superior storage capability for aqueous zinc-ion batteries, *J. Energy Chem.*, 2022, **67**, 645–654.

31 Z. Li, Y. Ren, L. Mo, C. Liu, K. Hsu, Y. Ding, X. Zhang, X. Li, L. Hu, D. Ji and G. Cao, Impacts of Oxygen Vacancies on Zinc Ion Intercalation in VO(2), *ACS Nano*, 2020, **14**, 5581–5589.

32 Z. Zhang, B. Xi, X. Wang, X. Ma, W. Chen, J. Feng and S. Xiong, Oxygen Defects Engineering of $VO_2{\cdot}xH_2O$ Nanosheets *via In Situ* Polypyrrole Polymerization for Efficient Aqueous Zinc Ion Storage, *Adv. Funct. Mater.*, 2021, **31**, 2103070.

33 Y. Liu, Y. Zhang, H. Jiang, J. Sun, Z. Feng, T. Hu, C. Meng and Z. Pan, Synergistic engineering of oxygen-defect and heterojunction boosts Zn^{2+} (De)intercalation kinetics in vanadium oxide for high-performance zinc-ion batteries, *Chem. Eng. J.*, 2022, **435**, 134949.

34 X. Liu, G. Xu, Q. Zhang, S. Huang, L. Li, X. Wei, J. Cao, L. Yang and P. K. Chu, Ultrathin hybrid nanobelts of single-crystalline VO_2 and Poly(3,4-ethylenedioxythiophene) as cathode materials for aqueous zinc ion batteries with large capacity and high-rate capability, *J. Power Sources*, 2020, **463**, 228223.

35 S. Wen, X. Gu, X. Ding, P. Dai, D. Zhang, L. Li, D. Liu, X. Zhao and J. Yang, Boosting Fast and Stable Alkali Metal Ion Storage by Synergistic Engineering of Oxygen Vacancy and Amorphous Structure, *Adv. Funct. Mater.*, 2022, **32**, 2106751.

36 S. Dong, Y. Li, M. Zhang, J. Wang, F. Li, S. Wu, P. Dai, T. Xing, X. Gu and M. Wu, Controllable engineering of intrinsic defects on carbon nanosheets enables fast and stable potassium storage performance, *Carbon*, 2023, **204**, 507–515.

37 W. Zhang, Y. Xiao, C. Zuo, W. Tang, G. Liu, S. Wang, W. Cai, S. Dong and P. Luo, Adjusting the Valence State of Vanadium in VO(2) (B) by Extracting Oxygen Anions for High-Performance Aqueous Zinc-Ion Batteries, *ChemSusChem*, 2021, **14**, 971–978.

38 Z. Cao, L. Wang, H. Zhang, X. Zhang, J. Liao, J. Dong, J. Shi, P. Zhuang, Y. Cao, M. Ye, J. Shen and P. M. Ajayan, Localized Ostwald Ripening Guided Dissolution/Regrowth to Ancient Chinese Coin-shaped VO_2 Nanoplates with Enhanced Mass Transfer for Zinc Ion Storage, *Adv. Funct. Mater.*, 2020, **30**, 2000472.

39 Z. Li, S. Ganapathy, Y. Xu, Z. Zhou, M. Sarilar and M. Wagemaker, Mechanistic Insight into the Electrochemical Performance of Zn/VO_2 Batteries with an Aqueous $ZnSO_4$ Electrolyte, *Adv. Energy Mater.*, 2019, **9**, 1900237.

40 X. Fan, X. Wen, Y. Tang, W. Zhou, K. Xiang and H. Chen, β-VO_2/carbon nanotubes core-shelled microspheres and their applications for advanced cathode in aqueous zinc ion batteries, *Electrochim. Acta*, 2021, **400**, 139425.

41 Z. Shi, Q. Ru, Z. Pan, M. Zheng, F. Chi-Chun Ling and L. Wei, Flexible Free-Standing VO_2/MXene Conductive Films as Cathodes for Quasi-Solid-State Zinc-Ion Batteries, *ChemElectroChem*, 2021, **8**, 1091–1097.

42 D. Pan, T. Liu, J. Fu and H. Liu, Superior electrochemical performance of dual-monoclinic δ-$NaxV_2O_5$/VO_2(B) composite material with enhanced synergistic effects, *J. Alloys Compd.*, 2022, **926**, 166952.

© 2023 The Author(s). Published by the Royal Society of Chemistry